CGI2013 manuscript No.
(will be inserted by the editor)

Three-dimensional Reconstruction using Multiresolution Photoclinometry by Deformation

Claire Capanna · Gilles Gesquière · Laurent Jorda · Philippe Lamy · Didier Vibert

Abstract We present a new photoclinometric reconstruction method based on the deformation of a 3D mesh. The optimization process of our method relies on a maximum-likelihood estimation with a density function measuring discrepancies between observed images and the corresponding synthetic images calculated from the progressively deformed 3D mesh. An input mesh is necessary and can be obtained from other methods or created by implementing a multiresolution scheme. We present a 3D shape model of an asteroid obtained by this method and compare it with the models obtained with two high-resolution 3D reconstruction techniques, stereophotogrammetry and stereophotoclinometry.

Keywords Photoclinometry · 3D reconstruction · Mesh deformation · Optimization · Multiresolution

1 Introduction

Three-dimensional shape reconstruction from images is a key problem in the field of computer vision. It consists in retrieving the 3D shape of the surface of objects from the variations of the pixels intensities in images of these objects. The two main families of methods developped in this field are stereography (hereafter stereo) and shape-from-shading (SfS).

We present here a new photoclinometry method which takes into account several images to reconstruct shape models thus combining the advantages of stereo and SfS. This method allows us to obtain a 3D shape model of any object presenting a uniform bi-directional reflectance. The surface must be seen from different directions and illuminated by a single point light source located at a distance from the object much greater than its size. The camera can in principle be located at any distance from the object given that the object represents at least ∼10 pixels across the image.

Our method is based on the deformation of a 3D triangular mesh in a non-linear optimization process. From the 3D mesh, synthetic images are created and this mesh is deformed until these synthetic images match the observed ones. This deformation is performed in a multiresolution scheme where the resolution of the mesh and the pixel scale of the images evolve in parallel.

Our method needs an input model described as a triangular mesh. This model can be a model obtained with another method (such as stereo, SfS or shape-from-silhouette [23]) or a simple geometric surface (such as a sphere or an ellipsoid).

After presenting related works in 3D reconstruction and in multiresolution (section 2), we describe in detail our reconstruction method (section 3) and show its application to the reconstruction of the asteroid (21) Lutetia (section 4).

2 Related works

We present below an overview of the 3D reconstruction methods implemented so far. We then focus on multiresolution schemes, often used in shape-from-shading.

C. Capanna (claire.capanna@lsis.org)
Aix Marseille Université, CNRS, LSIS (Laboratoire des Sciences de l'Information et des Systèmes), UMR 7296, Marseille, France

C. Capanna, L. Jorda, P. Lamy, D. Vibert
Aix Marseille Université, CNRS, LAM (Laboratoire d'Astrophysique de Marseille) UMR 7326, 13388, Marseille, France

G. Gesquière
Université Lumière, CNRS, Laboratoire LIRIS (Laboratoire d'InfoRmatique en Image et Systèmes d'information) , UMR 5205, Lyon, France

2.1 3D reconstruction from images

The first type of 3D reconstruction methods is binocular stereo which uses only two images. It has been studied for several decades [19] and has been extended to multi-view stereo [20]. Stereo methods calculate positions of stereo control points using a triangulation of corresponding points in several images. It is based on points and remarkable schemes detection, points matching and 3D control points calculation.
In astrophysics and geophysics, dense stereo is referred to as stereophotogrammetry (SPG). It correlates patches of a reference image in other images [8] in order to identify where the surface imaged in a patch of this reference image is observed in other images. SPG finds operations (translations, rotations, distortions) allowing to go from one image to the other so as to deduce the 3D topography of the observed object. Giese et al. [5] present a photogrammetry method in three steps: orientation parameters adjustment or rectification of images, conjugate points determination in the different images (correlation method using least squares minimization) and digital terrain models (DTMs) generation. Complex objects can be reconstructed but the conjugate points determination is always difficult to achieve, especially when the illumination of the scene changes from one image to the other because of the rotation of the object.

The second type of 3D reconstruction methods is shape-from-shading. This type of method was introduced by Horn [9] and has also been studied for decades [26]. It consists in determining the distribution of slopes of the surface facets of an object in a 3D scene from the intensity of the pixels. When an object is illuminated, the radiance reflected towards the observer depends on the observer and light source positions, as well as on the shape and reflectance properties of the object. Likewise stereo, SfS is an inverse problem (to find a 3D shape from 2D information) for which there is no unique solution unless several external constraints are introduced [16].
In astrophysics and geophysics, SfS is referred to as photoclinometry. Gaskell et al. [4] have developed a stereophotoclinometry (SPC) method calculating several control points and tiling the entire surface of an ofject in small DTMs of increasing resolution centered at these control points. From several images of a single area taken under different viewing and illumination conditions, this method has allowed to reconstruct models of several small bodies of our Solar System.

Nonetheless, both methods have limitations:

(i) The horizontal resolution of the SPG method is comparable to the size of the patches used to build the stereo control points, i. e., 5-10 times the pixel scale. The projected pixel scale of an image corresponds to the size of the area at the surface of the object imaged by a single pixel of the camera.

(ii) When the illumination and viewing conditions during the acquisition of the images are unfavorable, the SPC method tends to smooth out small scale topographic details which are interpreted by the algorithm as variations of the local reflectance properties (cf. Figure 1).

(iii) SPG and SPC both require images in which the object represents at least ∼100 pixels across to retrieve the 3D shape of the object.

(iv) In SPG, the silhouette is not taken into account during the reconstruction. In SPC, it is taken into account only if the surface responsible for the silhouette can be tiled with a DTM from other images (cf. Figure 2).

To overcome these limitations, these two methods are often used in conjunction, which leads to improve the accuracy of the reconstructed 3D models [25].

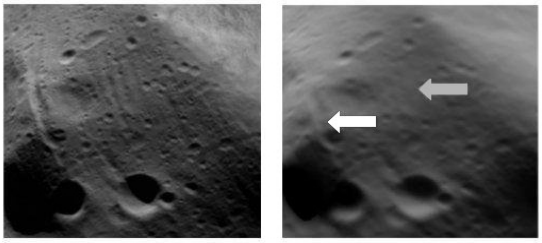

Fig. 1 Illustration of the problems with SPC reconstruction by comparing the observed image (left panel) of a small body and the synthetic image (right panel) created from the SPC 3D model. The arrows point to topographic details (grooves) which are absent in the synthetic image.

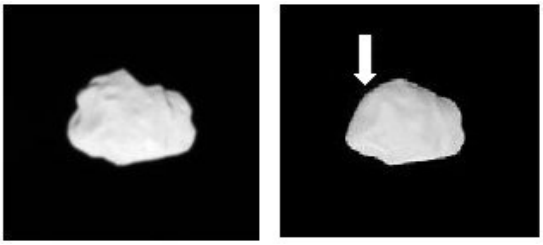

Fig. 2 Illustration of the silhouette problems with SPC reconstruction by comparing the observed image (left panel) of a small body of the Solar System and the synthetic image (right panel) created from the SPC 3D model. The arrow, in the synthetic image, points to parts of the silhouette which are not correctly reconstructed.

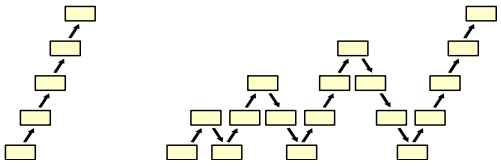

Fig. 3 "Cascading Multigrid" (left panel) and "Full Multigrid" (right panel) multiresolution schemes [1] .

2.2 Multiresolution

Multiresolution methods are often used in SfS to ensure the propagation of constraints across large representations [24]. Since increases (resp. reductions) of the spatial resolution of the 3D models imply reductions (resp. increases) of images pixel scales [15], multiresolution has to be applied to both 3D models and images.

There are different multiresolution schemes (e.g., [2]). Botsch et al. [1] demonstrate that a scheme which goes back and forth in resolutions provides a better quality result than the "Cascading Multigrid"(direct ascending scheme) illustrated on the left panel of Figure 3. Given a level of resolution R, the "Full Multigrid" scheme [1] consists in: (a) going back to the starting (lowest) resolution going through each intermediary level of resolutions, and then (b) using a direct ascending scheme to reach back the resolution R, once again going through each intermediary resolutions, before considering a new higher resolution $R+1$. This multiresolution scheme is illustrated on the right panel of Figure 3.

3 Multiresolution Photoclinometry by Deformation

Our reconstruction method belongs to the family of clinometry methods and consists in deforming of a 3D triangular mesh in a non-linear minimization process. From the 3D mesh, synthetic images are created and this mesh is deformed using the parameters p_k until the synthetic images $\mathbf{S}$ match the observed ones $\mathbf{O}$.
The objective function $\mathcal{F}$, that we minimize, combines two terms. The first term $L(\mathbf{O}, p_k)$ is minus the log of the maximum-likelihood of the parameters for quantifying the discrepancies between images. The second term is a prior penalty $S_C(p_k)$ used to enforce the smoothness of the mesh. We write:

$$\mathcal{F}(p_k) = L(\mathbf{O}, p_k) + S_C(p_k). \quad (1)$$

This function $\mathcal{F}$ is minimized at different resolutions. At each level of resolution, we use corresponding images with approximatively the same pixel scale.

We call our reconstruction method "Multiresolution Photoclinometry by Deformation" (MPCD). We present its flow chart in Figure 4. As a starting point, we consider a 3D shape described by a triangular mesh. This model can either be a sphere or a model obtained by another 3D reconstruction method when it is available.

The different steps of our reconstruction method (cf. Figure 4) are thus:
- the maximum likelihood estimation (L): the density function quantifies the discrepancies between images (cf. section 3.1)
- the smoothness constraint (S_C): the prior function prevents artifacts which can appear during the optimization process (cf. section 3.2)
- the deformation scheme: the choice of the set of parameters (p_k) triggers the model deformation and allows to maximize the likelihood function (cf. section 3.3)
- the optimization method: the algorithm chosen maximizes the likelihood (cf. section 3.4)
- the multiresolution scheme (cf. section 3.5).

3.1 Maximum likelihood estimation

Our problem corresponds to the maximization of the likelihood of a 3D shape model given noisy observations of an object. We model the observations by synthetic images and an additive gaussian noise $\mathbf{n}$ such as:

$$\mathbf{O} = \mathbf{S}(p_k) + \mathbf{n}. \quad (2)$$

This noise $\mathbf{n}$ is composed of the noise of the readout electronics, which is generally assumed to be gaussian,

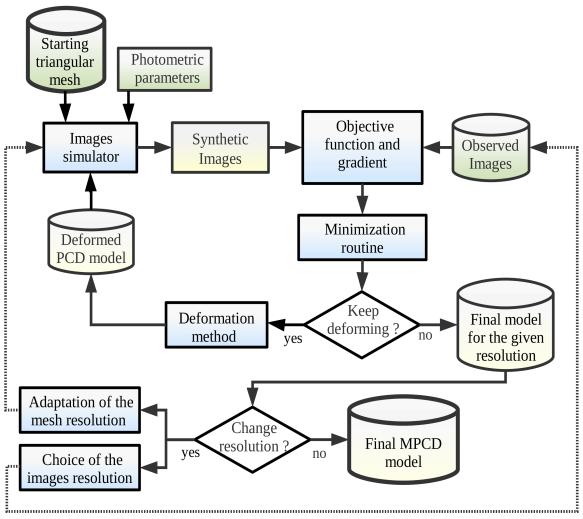

Fig. 4 Flow chart of our MPCD method. For more details, see section 3.

and the photon noise which follows a Poisson statistic. Generally, the signal values are large enough so that the Poisson noise can be approximated by a gaussian function and consequently, $\mathbf{n}$ becomes altogether a gaussian noise. Its standard deviation at each pixel m is:

$$\sigma_m(p_k) = g \cdot \sqrt{\frac{S_m(p_k) \cdot t_{exp}}{g} + \kappa^2} \tag{3}$$

with t_{exp} the exposition time of the image and g the gain of electronics. The first term under the square-root corresponds to photon noise [10] and the second term κ to the readout noise.

The probability of a gaussian noise with $\mathbf{N}$ its covariance matrix is $\mathcal{P}(\mathbf{n}) = exp(-1/2\mathbf{n}^t\mathbf{N}^{-1}\mathbf{n})$.
The likelihood of the parameters is $\mathcal{L}(p_k) = \mathcal{P}(\mathbf{O}|p_k)$. For a gaussian noise we can write:

$$\mathcal{L}(p_k) = exp\left(-\frac{1}{2}(\mathbf{O} - \mathbf{S}(p_k))^t\mathbf{N}^{-1}(\mathbf{O} - \mathbf{S}(p_k))\right) \tag{4}$$

If the noise is non correlated, we have $\mathbf{N} = diag(\sigma_m)$. Taking the *log*, we thus have:

$$L(p_k) = -2\log(\mathcal{L}(p_k)) = \sum_{m}^{N_{pix}} \frac{(O_m - S_m(p_k))^2}{\sigma_m^2(p_k)} \tag{5}$$

This function $L(p_k)$ is a non-linear function of the free parameters p_k which quantifies the differences between the N_{pix} pixels of the observed images and their synthetic counterparts. Hence, it takes into account both pixel variations in the illuminated part of the images due to changes of the slope and silhouette constraints.

3.2 Smoothness constraint

Our deformation scheme (cf. section 3.3) implies that the changes of the position of a vertex do not directly imply changes of the position of its neighbors. This may result in artifacts which are most pronounced in areas which are observed at the silhouette in at least one image. The bi-directional reflectance is not well determined in those areas and the large number of facets included in a pixel of the silhouette, combined with large values of the derivatives cause the optimization routine to create artifacts in these regions. This implies large displacement of such vertices and since the neighboring vertices are not forced to move, it creates artifacts. To prevent this problem, we add a prior $S_C(p_k)$ to the maximum-likelihood estimation, so as to force the slope of neighbouring facets to remain close from one another. This prior corresponds to a smoothness constraint given by:

$$S_C(p_k) = \alpha \frac{\sum_{i=1}^{F}\sum_{mi=1}^{3} |\mathbf{F}_{mi}(p_k) - \mathbf{F}_i(p_k)|^2 . S_{mi}(p_k)}{\sum_{i=1}^{F} S_i(p_k)} \tag{6}$$

for a model containing F facets where $\mathbf{F}_j$ is the normal of facet number j, S_j its surface, and mi describes the indexes of the 3 neighboring facets of facet number i.

The factor α, which allows to set the weight of the smoothness penalty relative to the maximum-likelihood, has been determined empirically to prevent artifacts without stopping the convergence of the maximum-likelihood term. We adopt a constant value of $\alpha = \mathcal{F}_o/(4S_{Co})$ with $\mathcal{F}_o$ given by (Eq. 1) at the beginning of the optimization and S_{Co} the initial smoothness constraint value with $\alpha = 1$. This leads to a value of the smoothness constraint (S_C) four times lower than the maximum-likelihood function (L) of the images at the beginning of the optimization.

3.3 Deformation scheme

A deformation scheme is used to modify the coordinates of the vertices of the three-dimensional mesh used to represent the surface of the body. The choice of this scheme defines the free parameters p_k. Our deformation scheme is based on a modification of the heights of the vertices along a pre-defined local direction. This direction is chosen parallel to the initial local normal $\mathbf{N^o}_k$, which is calculated by averaging the initial normal vectors of the facets which share this vertex. The free parameter p_k represents the displacement of the vertex number k along this direction $\mathbf{N^o}_k$. This direction is not updated during the optimization due to the small displacements at each iteration.

With $\mathbf{R^o}_k$ the initial position of vertex k, the coordinates $\mathbf{R}_k$ of this vertex after deformation become:

$$\mathbf{R}_k = \mathbf{R^o}_k + p_k\ \mathbf{N^o}_k. \tag{7}$$

3.4 Optimization method

To minimize the objective function $\mathcal{F}$ (Eq. 1), we use a non-linear optimization routine based on the "limited memory Broyden - Fletcher - Golbfarb - Shanno with boundaries" (L-BFGS-b) algorithm [13], a quasi-Newton method [3] especially designed for large-scale convex problems. Other methods, such as [14] and [6],

have also been tested, but we found L-BFGS-b to converge to lower values of the function in our case. It also allows to set lower and upper boundaries for each parameter.
In order to find a function f extrema, Newton methods define a sequence x_i such as:

$$x_{i+1} = x_i - \underbrace{[\nabla^2 f(x_i)]}_{Hessian\ matrix}^{-1} . \underbrace{\nabla f(x_i)}_{Gradient} . \quad (8)$$

Quasi-Newton methods use the sequence:

$$x_{i+1} = x_i - \alpha_i . [\nabla^2 f(x_i)]^{-1} . \nabla f(x_i) \quad (9)$$

with α_i a coefficient chosen to optimize the convergence. As Newton methods, quasi-Newton methods allow to find the extrema of a function but the second derivatives of the Hessian matrix do not need to be calculated. We define d_i the search directions at iteration i such as: $d_i = -[\nabla^2 f(x_i)]^{-1} . \nabla f(x_i)$ and $x_{i+1} = x_i + \alpha_i d_i$. We thus have $B_i . d_i \approx -\nabla f(x_i)$.
The estimation B_i of the Hessian matrix can thus be uploaded with successive analyses of the gradient. Quasi-Newton methods give: $B_{i+1} = \eta_i . B_i + U_i$ and in the case of BFGS we have:

$$\begin{cases} \eta_i = 1 \\ U_i = \dfrac{y_i . {}^t(y_i)}{{}^t(y_i) . s_i} - \dfrac{B_i . s_i . {}^t(s_i) . B_i}{{}^t(s_i) . B_i . s_i} \end{cases} \quad (10)$$

with $s_i = x_{i+1} - x_i$ and $y_i = f(x_{i+1}) - f(x_i)$.

The L-BFGS-b procedure thus requires the calculation of the first order partial derivatives ($\nabla f(x_i)$) of the function to minimize. The method can converge after a low number of function and gradient evaluations. This is particularly important in our case since those evaluations are highly time-consuming.
The convergence is achieved when at least one of the two following conditions are met: (i) the difference of the function values between two iterations is lower than a threshold, (ii) the difference of the maximum value of the gradient between two iterations is lower than another threshold (*http://users.eecs.northwestern.edu/~nocedal/lbfgsb.html*). These thresholds are both parameters of the L-BFGS-b procedure.

It is important to note that, like any quasi-Newton method, L-BFGS-b is guaranteed to converge to a global solution only if the function is convex.

3.5 Multiresolution scheme

Our objective function $\mathcal{F}$ is unfortunately non necessarily convex which means that the minimization method using L-BFGS-b can lead us to a local minimum. In order to overcome this problem we use a multiresolution scheme. At coarse resolution the function tends to become more convex.

Our multiresolution scheme is inspired by the "Full Multigrid" method. The only difference is that we go back only to the level of resolution just below the current level while the "Full Multigrid" method consists in going back to the starting (lowest) resolution. The multiresolution scheme allows to avoid local minima since going back to a coarser resolution removes small local minima and thus tends to find the global minimum with L-BFGS-b.

For a 3D shape model, going from one resolution to the next one can be achieved with mesh subdivision [12] and going down in resolution with reverse subdivision [18]. For images, only going down in resolution is feasible, large pixel scale images can indeed be calculated from low pixel scale images. For this, we use the binning method, which consists in averaging the values of a group of 2x2 pixels.

At each resolution, we reconstruct the shape with an accuracy proportional to the projected pixel scale of the observed images.

The highest resolution level reachable by the method is currently limited by the computational time. We reach the last step when the number of pixels and facets is so large that the computational time becomes prohibitive. Another method will then be used to retrieve the topography at higher resolution. This method will use a division of the global model into small surface elements so as to generate local DTMs, following the approach introduced by Gaskell et al. [4]. The optimization of these DTMs will be done with the same optimization process. This extension of the method will be described in a forthcoming article.

4 Results: Lutetia 3D reconstruction

We used several small solar system bodies to test our method. We choose here to only present the results given with our case study of the asteroid (21) Lutetia which has also been reconstructed with other methods.

The asteroid (21) Lutetia was observed during a flyby by the Rosetta spacecraft of the European Space Agency (ESA). The Rosetta spacecraft includes the imaging experiment OSIRIS (Optical, Spectroscopic, and Infrared Remote Imaging System).

4.1 Image selection criteria

The CCD images are acquired by a single moving camera while the object rotates. They are processed to re-

move radiometric and geometric instrumental effects. A set of images taken with the same colored filter is extracted according to three criteria. A new image is selected if: (i) the distance between the object and the camera varies by a factor of at least 1.5, or (ii) the viewing angle varies by at least 10°, or (iii) the illumination angle varies by at least 10°. This scheme ensures that the selected images are sufficiently different one from another, thus bringing enough new information to the algorithm.

A sub-set of 27 images of Lutetia, extracted from the whole set of 400 images acquired by the camera, is selected according to the above mentionned criteria. For these images, the spacecraft-object distance decreases from 510,000 km (image #1) to 3,170 km (image #20) at closest approach, and increases again to 6,100 km (image #27) later on. The corresponding projected pixel scales are respectively 9.70 km, 60 m and 115 m. The phase angle varies from 10° (image #1) to 140° (image #27). The phase angle is the angle between the Sun direction and the spacecraft direction, as seen from the center of the object. Six of the 27 selected images of Lutetia are presented in Figure 5, where the pixel scale varies from $\sim$ 4 km (top left panel) to 60 m (bottom left panel).

4.2 Application of MPCD

The synthetic images (cf. Section 3.1) are created by a tool called OASIS (Optimized Astrophysical Simulator for Imaging Systems, [10]). OASIS considers a shape model described by a triangular mesh. It calculates the position and the orientation of the object in the camera frame as a function of time.

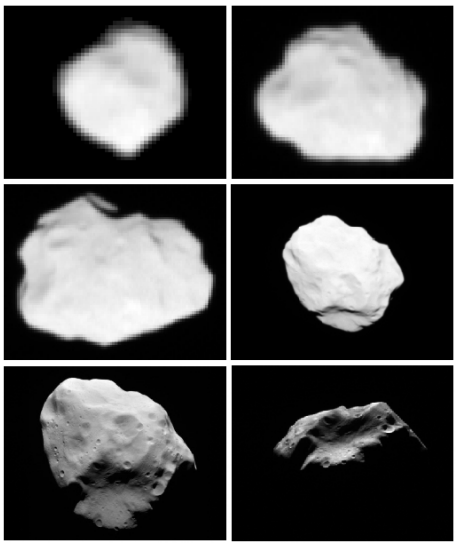

Fig. 5 Example of 6 images with different pixel scales used for the 3D reconstruction (case of asteroid Lutetia).

To start our reconstruction, we need high pixel scale images. To obtain such images, we progressively rebin each selected image up to the pixel scale needed to perform the first step of the multiresolution scheme and keep the intermediary binned images for upper levels of resolution. The images already at this pixel scale are not rebinned.

After this binning, we thus have n subsets of images corresponding to n different pixel scales with n depending on the range of pixel scales in the subset. If we note A the largest pixel scale and B the lowest, we have n such as $A \simeq 2^n B$. In Figure 6, $A \simeq 20$ km (bottom row), $B \simeq 1.24$ km (top row) and $n = 5$ (number of rows). The first subset of images constains 27 un-binned and binned images corresponding to the highest pixel scale, the second subset only contains 26 images and the following subsets 24 images. The subsets contain decreasing numbers of images because the low pixel scale images corresponding to the level of resolution does not always exist.

We apply our multiresolution method of photoclinometry by deformation (MPCD, cf. Figure 4) to reconstruct the shape of the asteroid Lutetia with 5 levels of resolution (cf. Figure 6). This case study implies a very good knowledge of the positions of the camera and the object as well as an optimization of their orientation parameters. These parameters are optimized, apart from the heights of vertices, with the same maximum-likelihood computation (Section 3.1). The values χ given in Figure 6 correspond to the sum of absolute value of the differences between observed and synthetic images:

$$\chi = \sum_{m}^{N_{pix}} \mid O_m - S_m(p_k) \mid . \tag{11}$$

It represents the discrepancies between these images given in units of the instrumental noise (σ). Computational times given in Figure 6 correspond to a parallelized code running on an Intel Xeon CPU of 3.20GHz with a 8 GB RAM and 4 cores. In this section, we first show our results and justify with examples our different choices and especially the use of our multiresolution scheme. We then compare our results with those of other methods: SPC and SPG [17] (see Section 2.1).

The body rotates during the flyby, which allows us to image all the surface illuminated during one rotation cycle of the asteroid. However, about 25 % of the surface is not imaged because the spin axis is not perpendicular to the orbital plane which contains the light source (the Sun).

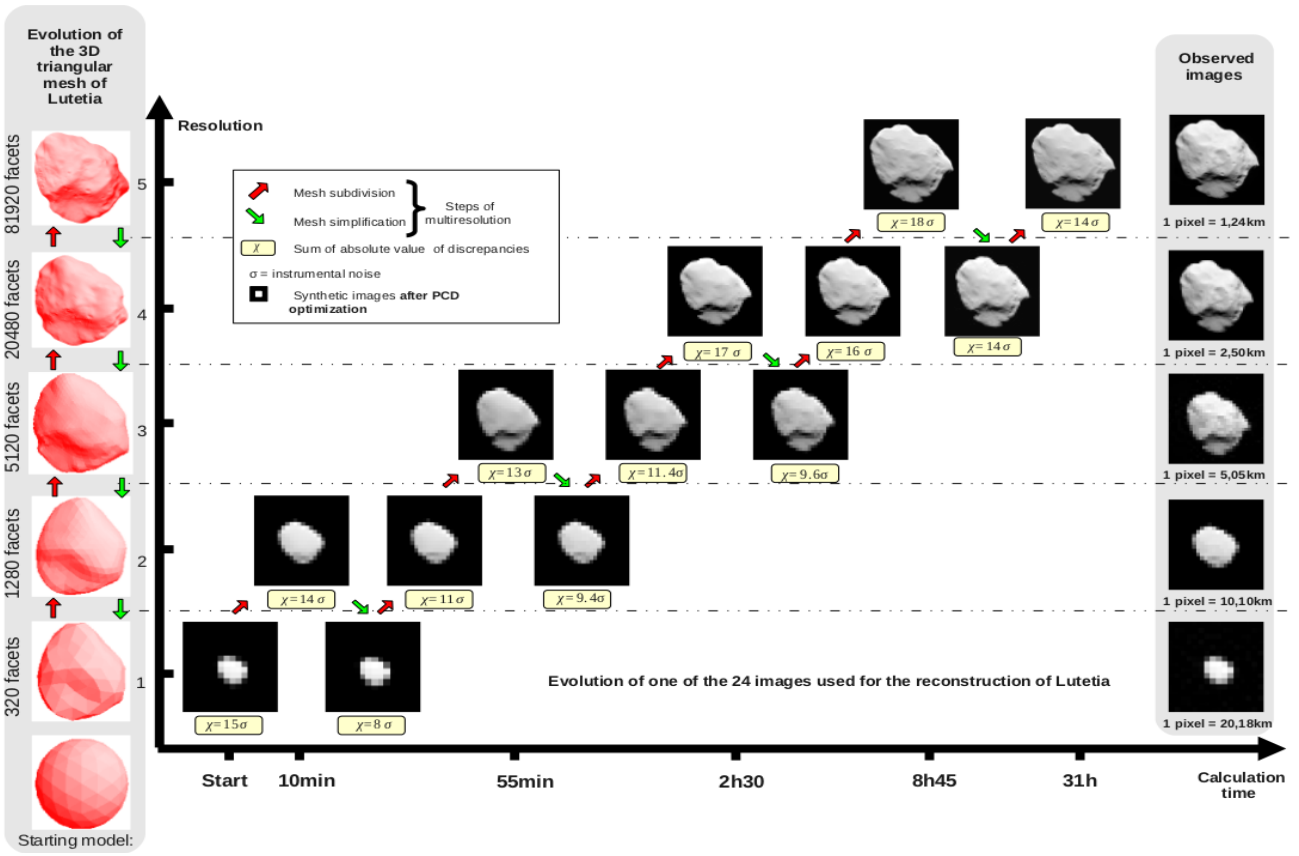

Fig. 6 Steps of the multiresolution scheme: evolution of the images and the shape model.

As starting point, we use a 120 km-diameter sphere built from an icosahedron [22]. This size of the sphere is estimated from previous studies of the object: e. g. Lamy et al. [11] estimate a size of ∼130 x 100 x 95 km. With this very low resolution model (level 1, first bottom row of Figure 6) containing 320 facets, we use the whole first subset of images corresponding to the largest pixel scale. We deform this model using our optimization method with the smoothness constraint The model is then subdivided to obtain the level 2 (second row of Figure 6) of resolution and optimized with the corresponding subset of 26 images. For level 3, level 4 and level 5 (third, fourth and fifth rows of Figure 6) of our multiresolution scheme, the corresponding subsets of 24 images are used.

The steps of our multiresolution scheme are illustrated in Figure 6 where we can see that smaller topographic details are reconstructed when we decrease the pixel scale of the images. Our method allows us to reconstruct entirely the 74% of the surface of Lutetia observed during the flyby, . Lutetia dimensions are approximatively 121 x 101 x 75 km [21], this prooves that our reconstruction method is efficient eventhough the shape is not exactly spherical and the starting sphere is not a good approximation of the shape of the object.

4.3 Validation of our method

Figure 7 presents one of the 24 images used for our level 5 optimization.

Figure 8 presents the results of the method when no multiresolution scheme is used, i.e., when we directly optimize the sphere at high resolution with low pixel scale images.

For each pixel m of image n, we can calculate the residual value in units of instrumental noise:

$$\rho_m^{(n)} = \frac{O_m^{(n)} - S_m^{(n)}(p_k)}{\sigma_m^{(n)}} \tag{12}$$

The resulting residual images allow an easy visualization of the differences between the observed and synthetic images.

Without multiresolution, the limbs (silhouettes) of the asteroid are not correctly reconstructed. Indeed on the top of the residual image (Figure 8, right panel), we can see that several neighboring pixels have a very low grey value which proves that the model presents a limb that is too smooth and does not create the trough that is visible in the observed image of Figure 7. This result proves that, without multiresolution, the minimization with L-BFGS-b reaches a local minimum which does

Fig. 7 One of the selected observed image using during Lutetia reconstruction using MPCD.

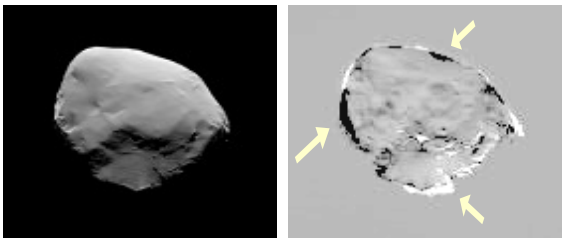

Fig. 8 One of the synthetic image from the model (left panel) obtained with our method without using multiresolution and corresponding residual image (right panel). The arrows show the main problems.

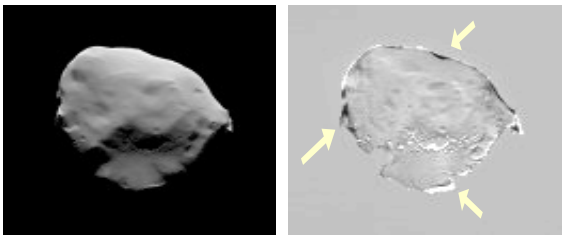

Fig. 9 One of the synthetic image from the model obtained using the Cascading Multigrid scheme (left panel) and corresponding residual image (right panel). The arrows show the main problems.

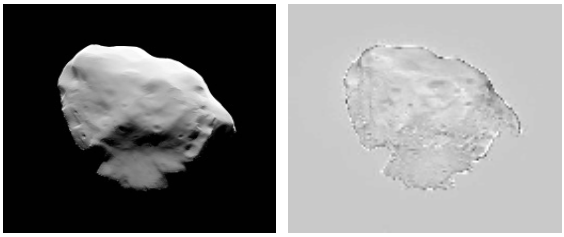

Fig. 10 One of the synthetic images from our MPCD model (left panel) and corresponding residual image (right panel).

not correspond to the best fit of parameters.
Figure 9 shows the result of the "Cascading Multigrid" scheme. Even though this result is better than the one with no multiresolution scheme, the limbs are still not very well retrieved. Large white and black areas are indeed visible in the corresponding residual image (Figure 9, right panel).
Figure 10 presents the results of our MPCD method. The synthetic image of Figure 10 can be compared with

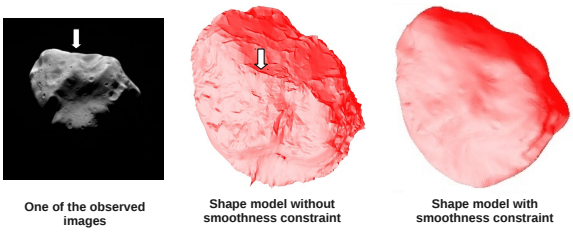

Fig. 11 Example of a mesh obtained without (middle panel) and with (right panel) a smoothness constraint after an optimization with 8 images. The white arrow on the observed image (left panel) shows the silhouette that creates the artifact on the shape model also shown by a white arrow.

the observed image of Figure 7, we can see that regardless high resolution details the surface is correctly reconstructed. The residual image (Figure 10, right panel) confirms this results since no large white and black areas are visible. Nevertheless, we can see that with our method there are still some problems with the topography of the asteroid. For example, several craters are visible on the residual images which means that they are not perfectly reconstructed. Black and white pixels m correspond to a residual value $\rho_m = \pm\ 12\ \sigma_m$ in Figures 8–10. The use of the "Full Multigrid" scheme gives the same results as our multiresolution scheme. The only difference is an increase of the computational time with the "Full Multigrid" scheme.
Figure 11 illustrates the difference of models obtained with and without smoothness constraint (see Section 3.2) during the tests on the reconstruction of Lutetia. The improvement speaks for itself.

4.4 Comparison with other methods

In order to test the accuracy of our method, we perform a quantitative comparison of the low-resolution model of Lutetia retrieved with the MPCD method with high-resolution models of the same object obtained with the SPC and SPG methods (Figure 12). These two models have an uncertainty of about 40 m in elevation above the surface and a spatial resolution of about 100 m. We point out that, unlike the MPCD model presented

Fig. 12 Comparison between our MPCD model (left), the SPC model (center) and the SPG model topography reconstruction (right).

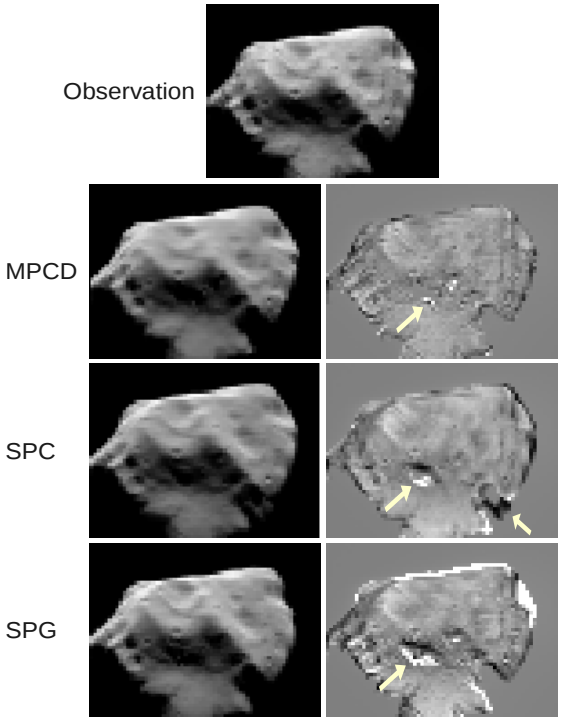

Fig. 13 Comparison between our method MPCD, SPC and SPG: topography reconstruction. Observed image (1st row), synthetic (left pannel) and residual images (right panel) from our MPCD model (second row), from the SPC model (third row) and from the SPG method (fourth row). The arrows show the main problems.

here, the SPC and SPG models have been reconstructed using purely un-binned images with the lowest possible pixel scale of 60 m at the closest approach. For this comparison, we generate 27 synthetic images corresponding to those used to build the MPCD model, but using as input the SPC and SPG shape models of Figure 12. We also calculate the corresponding residual images. Residual images of the SPC and SPG models are shown in Figure 13 respectively, where black and white pixels m in residual images correspond to a residual value $\rho_m = \pm\ 8\ \sigma_m$. We also quantify the local distance between two models using the "CloudCompare" tool [7]. This tool also provides us with the histogram of the distribution of local distances. The comparison is shown in Figures 15 and 16.

The MPCD model has the lowest image residuals of the three methods, but a few pixels near projected shadows still have large residuals (Figure 13, first row left panel). The topography around areas in shadow is more accurately modeled by MPCD. The histograms of local distances (Figures 15 and 16, right panels) are both well-described by a Gaussian distribution. We can see on Figures 15 and 16 that the differences between the MPCD model and the SPG and SPC models present clear similarities. As an example, part of the rim of the large crater at the center of the models is higher in both models (yellow-orange patches). Figures 15 and 16 indicate that, apart from these specific locations our MPCD model is mainly affected by errors of less than 1 km. We stress that these errors still remain lower than the pixel scale (between 20.2 and 1.24 km) of the images used to reconstruct the MPCD shape model.

The MPCD method reproduces the limb of the object slightly better than the SPC method (Figure 13 , second and third row). This is also illustrated in Figure 14, in which the observed limb is better reproduced with the MPCD model than with the SPC one. The SPC model covers 60 % of the surface, slightly less than the MPCD model (74 %). The corresponding histogram (Figure 15) can be compared to a gaussian function centered at -0.2 with a standard deviation of 0.8.

The SPG model only covers 36% of the object. The corresponding histogram (Figure 16) can be compared to a gaussian function centered at zero with a standard deviation of 0.6. Note however that the two models have a slightly different surface coverage.

5 Conclusion and future work

We develop a new multi-image photoclinometry method (MPCD) based on local deformations of a three-dimensional shape model. The deformation is guided by the minimization of the differences between a set of observed images of the object and their synthetic counterparts, generated from the deformed shape model. We use a multiresolution scheme to ensure a better accuracy of the final reconstructed shape model. This method is applied to a set of 27 images of the asteroid Lutetia observed during a flyby of the asteroid by the ROSETTA spacecraft. We successfully reconstruct a model which covers the whole surface imaged by the camera aboard ROSETTA. The accuracy of this model is equal to ~ 0.5 times the minimum pixel scale of the observed images.

Fig. 14 Comparison between our method MPCD and SPC: limbs reconstruction. Observed image (left panel), synthetic images from our MPCD model (center panel) and from the SPC model (right panel). The arrow shows the main problem.

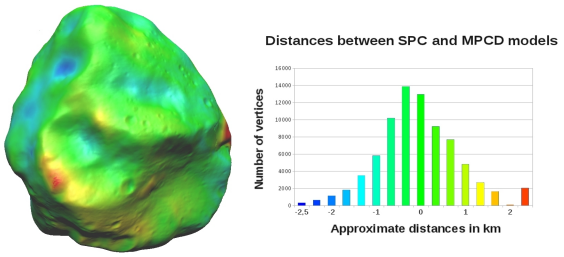

Fig. 15 Image of the distance in km between the MPCD and the SPC models (left panel) and histogram of these distances (right panel).

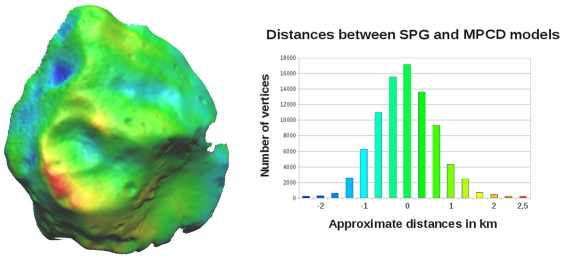

Fig. 16 Image of the distance in km between the MPCD and the SPG models (left panel) and histogram of these distances (right panel).

We compare our MPCD model with those derived with the SPC and SPG techniques. The MPCD method allows to model a larger fraction of the surface (74 % instead of 36–60 %). It also allows to better reproduce the limb of the object on images, and the topography near shadowed areas.

Our final goal is the reconstruction of the shape at a spatial resolution comparable to the lowest pixel scale of images acquired by the camera. For this, we will segment the model into smaller DTMs and optimize each of them with our MPCD technique before merging them into a global shape.

References

1. M. Botsch et al., Geometric modeling based on polygonal meshes, Proc. ACM SIGGRAPH, (2007)
2. W. Briggs, S. McCormick, Multigrid methods, series: Frontiers in applied Mathematics, SIAM, (1987)
3. R. Byrd, J. Nocedal, R. Schnabel, Representation of quasi-Newton matrices and their use in limited memory methods, Mathematical Programming, v. 63, n. 4, p. 129-156 (1994)
4. R. Gaskell et al., Characterizing and navigating small bodies with imaging data, Meteoritics and Planetary science, v. 43, p. 1049-1061 (2008)
5. B. Giese,J. Oberst, R. Kirk, W. Zeitler, The Topography of Asteroid Ida: A Comparison between Photogrammetric and Two-dimmensional Photoclinometric Image Analysis, Int. Arch. of Photogram. and Remote Sens., v. XXXI, p.245-250 (1996)
6. P. E. Gill,W. Murray and M. H. Wright, Practical Optimization, Academic Press (1981)
7. D. Girardeau-Montaut et al., Change Detection on Points Cloud Data acquired with a Ground Laser Scanner, ISPRS Workshop Laser Scanning III/3, p. 30-35 (2005)
8. K. Gwinner et al., Derivation and validation of highresolution digital terrain models from mars express HRSC-Data, Photogramm. Eng. Remote Sens., p. 1127-1142 (2007)
9. B.K.P. Horn, Shape from Shading : A Method for Obtaining the Shape of a Smooth Opaque Object from One View, PhD thesis, MIT (1970)
10. L. Jorda, S. Spjuth, H.U. Keller, P. Lamy, A. Llebaria, OASIS: a simulator to prepare and interpret remote imaging of solar system bodies, Proc. SPIE, v. 7533 (2010)
11. P. L. Lamy, G. Faury, L. Jorda, M. Kaasalainen and S. F. Hviid, Multi-color, rotationally resolved photometry of asteroid 21 Lutetia from OSIRIS/Rosetta observations, Astronomy and Astrophysics, v. 521, p. 19 (2010)
12. C. T. Loop, Smooth Subdivision Surfaces Based on Triangles, M.S. Thesis, University of Utah, (1987)
13. J.L Morales, J. Nocedal, Remark on "Algorithm 778: L-BFGS-B: Fortran subroutines for large-scale bound constrained optimization". ACM Trans. Math. Softw. v.38(1), p. 1–4 (2011)
14. J. More, The Levenberg-Marquardt algorithm: Implementation and theory, Numerical Analysis, v. 630, p.105-116 (1978)
15. S. Peleg, G. Ron, Nonlinear Multiresolution : A Shape-from-Shading Example, IEEE Transactions on Pattern Analysis and Machine Intelligence, v. 12, n. 12, 1206-1210 (1990)
16. E. Prados, O. Faugeras, F. Camilli, Shape from shading: a well-posed problem?, Research report 5297, Institut National de Recherche en Informatique et en Automatique, Sophia Antipolis, France (2004)
17. F. Preusker et al., The northern hemisphere of asteroid 21 Lutetia topography and orthoimages from Rosetta OSIRIS NAC image data, Planetary and Space Science, v. 66, p.54-63 (2012)
18. F. Samavati, H. Pakdel, C. Smith and P. Prusinkiewicz, Reverse Loop Subdivision, Tech. rep. 2003-730-33, University of Calgary, (2003)
19. D. Scharstein, R. Szeliski, A taxonomy and evaluation of dense two-frame stereo correspondance algorithms, International Journal of Computer Vision, v. 47, p. 7-42 (2001)
20. S. M. Seitz, B. Curless, J. Diebel, D. Scharstein, R. Szeliski, A comparison and evaluation of multi-view stereo reconstruction algorithms, Proc. CVPR, p. 519-528 (2006)
21. H. Sierks et al., Images of Asteroid 21 Lutetia: A Remnant Planetesimal from the Early Solar System, Science, v. 334, pp. 487-490 (2011)
22. A. Szalay et al., Indexing the sphere with the hierarchical triangular mesh, Tech. Rep. MSR-TR-2005-123, Microsoft Research (2005)
23. M. Tarini, M. Callieri, C. Montani, C. Rocchini, Marching Intersections: An efficient Approach to Shape-from-Silhouette, Conference on Vision, Modeling, and Visualization proceedings, p. 255-262 (2002)
24. D. Terzopoulos, Efficient Multiresolution Algorithms for Computing Lightness, Shape-from-Shading, and Optical Flow, AAAI-84 Proceedings, (1984)
25. C. Wu, B. Wilburn, Y. Matsushita, C. Theobalt, High-quality shape from multi-view stereo and shading under general illumination, IEEE Conference on Computeur Vision and Pattern Recognition, p. 969-976 (2011)
26. R. Zhang, P. Tsai, J. Edwin, M. Shah, Shape from Shading : A Survey, IEEE Transactions on Pattern Analysis and Machine Intelligence, v. 21, n. 8, p.690-706 (1999)